without any input voltage. However, the displacement of the output beam can be transferred to the actuator arrays through the vertical beams. This will induce an error of 0.1 μm in the output displacement. To solve this problem, two opposite groups of actuators or bidirectional actuators can be utilised so that the actuator array can deflect either left or right, depending on where the driving voltage is applied.

Simulation and design optimisation: Using an FEA software ANSYS™, the model of a four-bit WSDAC was studied. The maximum error deviated from the ideal was 1% of the maximum displacement. As a result, this DAC could hardly be extended to more bits. Several factors are thought to be the causes of the error. The displacement of the thermal actuator has both useful lateral and harmful vertical displacement, the flexure of the vertical beams is not completely linear, and the output beam is not absolutely rigid.

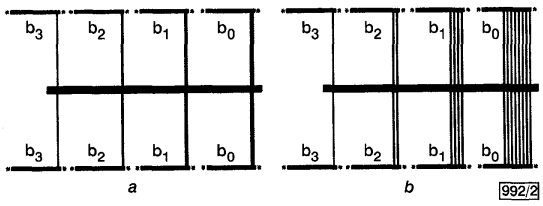

Fig. 2 *Diagram of symmetric WSDAC*
a Vertical beams of different widths
b Vertical beams of identical widths

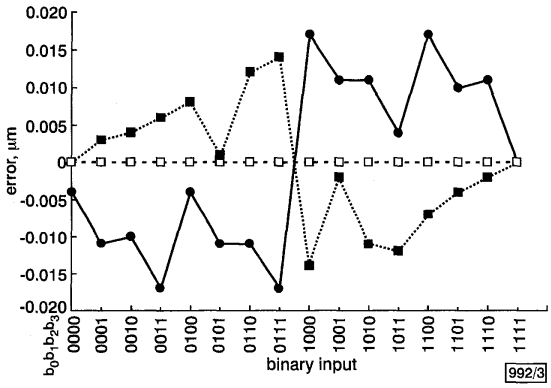

Fig. 3 *Errors of WSDAC and C-2C DAC*
···■··· WSDAC (Fig. 2*a*)
–□– WSDAC (Fig. 2*b*)
—●— C-2C DAC

Owing to the preliminary results, the original WSDAC design had to be modified. As is shown in Fig. 2*a*, the asymmetric structure was replaced by a symmetric one that includes eight vertical beams and eight actuator arrays. By removing the fixing beams, η was 1 in the formula, so the displacement of the output beam increased to 4 μm. The width of the output beam broadened. The modified WSDAC was analysed and the maximum error was 0.014 μm, which is equivalent to 0.35% of the maximum output displacement. To improve the accuracy, an optimised structure employing the number of the beams as the scale factor (Fig. 2*b*) was provided. Each actuator array was connected to 1, 2, 2^2 or 2^3 vertical beams of identical width and stiffness. The error of the model was shown to be less than 0.001 μm by FEA. The error was significantly less because the flexure nonlinearity of each vertical beam was equal. For the sake of comparison, the model of a symmetric C-2C DAC [2 – 4] was also analysed, in which the widths of the output beam and the vertical beams were equal to those of the WSDAC. The error of the C-2C DAC was 0.017 μm, while the maximum displacement was 3.75 μm. The errors of the three models are plotted in Fig. 3.

Conclusions: A model of a weighted-stiffness DAC has been proposed for the first time. Both the width and the number of the lateral beams were used to produce different stiffness, while the latter could be employed for nanopositioning. This DAC has the potential to be used in microrobotics, MOEMS, STM probe and data storage systems.

Acknowledgment: This project has been supported by the National Natural Science Foundation of China under Grant No. 60076028, and also by the PhD Program Foundation of the Education Ministry under Grant No. 2000028620.

9 April 2001
Electronics Letters Online No: 20010528
DOI: 10.1049/el:20010528

Qingquan Liu and Qing-An Huang (*Microelectronics Center, Southeast University, Nanjing 210096, People's Republic of China*)

E-mail: mems@seu.edu.cn

References

1 YEH, R., CONANT, R.A., and PISTER, K.S.J.: 'Mechanical digital-to-analog converters'. Proc. Transducers '99, 1999, pp. 998–1001
2 TOSHIYOSHI, H., KOBAYASHI, D., MITA, M., HASHIGUCHI, G., FUJITA, H., ENDO, J., and WADA, Y.: 'A digital-to-analog converter of displacement by an integrated micromechanism', *Jpn. J. Appl. Phys.*, 1999, **38**, (2), pp. 593–595
3 TOSHIYOSHI, H., KOBAYASHI, D., MITA, M., HASHIGUCHI, G., FUJITA, H., ENDO, J., and WADA, Y.: 'Micro-electro-mechanical digital-to-analog converter (MEMDAC)'. Proc. Transducers '99, 1999, pp. 947–957
4 TOSHIYOSHI, H., KOBAYASHI, D., MITA, M., HASHIGUCHI, G., FUJITA, H., ENDO, J., and WADA, Y.: 'Microelectromechanical digital-to-analog converters of displacement for step motion actuators', *IEEE/ASME J. Microelectromech. Syst.*, 2000, **9**, pp. 218–225
5 HUANG, Q.A., and LEE, N.K.S.: 'A simple approach to characterizing the driving force to polysilicon laterally driven thermal microactuators', *Sens. Actuators*, 2000, **A80**, pp. 267–272

Hybrid opto-mechanical gyroscope with injection-interferometer readout

M. Norgia and S. Donati

A hybrid micromachined-optoelectronic mechanical system (MOEMS) gyroscope is proposed. It consists of an electrically excited micro-mechanical resonator and an optical readout performed by a laser diode operating as an injection interferometer. An analysis of the system, validated by preliminary experimental results, indicates an attainable performance of 1 deg/h√Hz.

Introduction: A new gyroscope concept is presented. The gyroscope comprises a hybrid structure with an MEMS-like mechanical resonator to sense the inertial Coriolis force, combined with an optical readout performed by an injection interferometer. Compared with the capacitive sensing of a conventional MEMS gyroscope, the proposed approach is potentially more sensitive and has less noise. Also, it can be fabricated without the constraints imposed by the on-board capacitive readout, while retaining the potentially very small size and performance scalability. This feature makes the hybrid-MOEMS approach attractive for a number of medium-accuracy gyro applications, such as in the robotics and automotive sectors.

Analysis: A model of the mechanical section is shown in Fig. 1, where a mass M is suspended by springs with an elastic constant k_x along the x-axis, and k_z along the sensing axis. The mass is excited along the x-axis with a vibration amplitude Δx at frequency $f_x = \omega_x/2\pi$, reaching a peak velocity $v_x = \omega_x \Delta x/2$. When the system rotates with an angular velocity Ω_y directed along the y-axis, the Coriolis force $F_z = 2Mv_x\Omega_y$ generates an oscillation of the mass along the z-axis with amplitude $\Delta z \cong Q_z F_z/k_z$, where Q_z is the quality factor of the oscillator. The angular velocity can then be found from the measurement of Δz as

$$\Omega_y = \frac{k_z/M}{Q_z\omega_x\Delta x}\Delta z = \frac{\omega_{Rz}^2}{Q_z\omega_x\Delta x}\Delta z = \frac{\omega_{Rz}}{Q_z\Delta x}\Delta z \quad (1)$$

where $\omega_{Rz} = \sqrt{(k_z/M)}$ is the resonance frequency of the z-axis at which the device is excited ($\omega_x = \omega_{Rz}$).

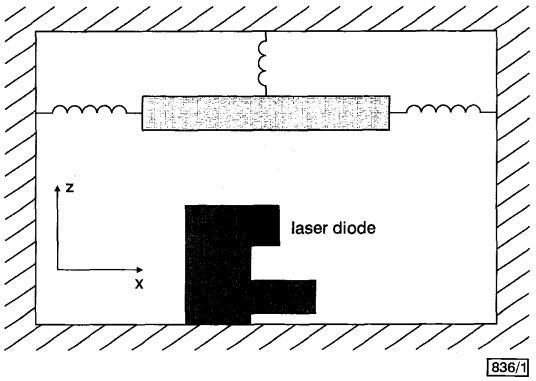

Fig. 1 *Hybrid gyroscope scheme*

To validate the hybrid gyro concept, we used a MEMS resonator (non-optimised, as intended for a different application), i.e. a 600 × 100 μm Si-mass suspended by four Si-springs and connected to two sensing-capacitor combs (see Fig. 2). In our setup, vibration along the x-axis was obtained by applying a sinusoidal drive voltage (typically 0 to +5 V) to the combs.

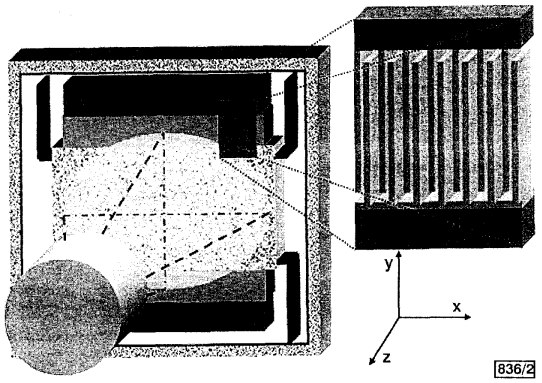

Fig. 2 *Experimental setup for hybrid gyroscope*

Laser diode and Si-mass suspended by four Si-springs. The capacitor comb is shown in detail on the right

Readout: An injection interferometer was used to sense the mass vibration along the z-axis. The working principle of this interferometer is described in detail in a number of previous papers [1 – 3]. Also, it has been successfully demonstrated for measuring the mechanical parameters of an MEMS [4]. The principle involves allowing the retro-reflection from the target under test to be injected back into the laser source, thus generating amplitude modulation of the laser power, of the type $P = P_0[1 + m\cos(2kz)]$ for a low injection level [2], where m is a modulation coefficient dependent on the optical attenuation experienced as a result of back and forth propagation (typically < 1%), and $2kz$ is the optical phase-shift of the field for propagation to a target distance z. Key features of the method, especially attractive for sensing hybrid structures and MEMS, are: (i) there is no need for external parts or critical alignment, as the laser itself filters out the single spatial mode re-entering the cavity; (ii) it can be used for weakly reflecting as well as diffusive target surfaces; (iii) the photodiode placed on the laser rear mirror is fully adequate for detection (no stray-light filtering is required); (iv) sub-nm sensitivity is easily achieved up to several hundreds of kHz.

Experimental results: In our setup, we used a Hitachi laser diode (HL7851G), rated at 50 mW power and used at 30 mW, emitting at λ = 780 nm, placed in front of the oscillating mass (see Fig. 2). The rear photodiode of the laser package was backed by an R = 200 kΩ transimpedance preamplifier.

To determine the interferometer sensitivity, a vibration along the z-axis was produced by a sinusoidal drive applied between the mass and the substrate. Fig. 3 displays the frequency spectrum of the interferometric signal when the mass vibrates with a Δz = 100 nm amplitude, compared with the spectra of the electronic noise (laser turned off) and of the instrument noise-floor. Here, the distance between laser output mirror and device mass was 1 mm (as limited by the laser package), and the laser spot on the mass was ≃ 150 × 400 μm. The MEMS surface was untreated, i.e. an almost Lambertian rough-surface.

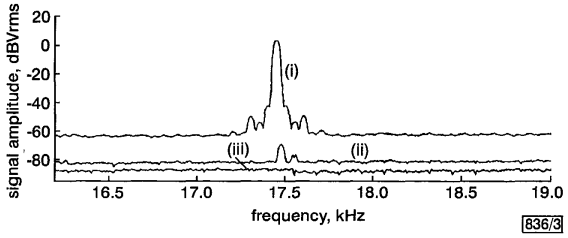

Fig. 3 *Interferometric signal spectrum compared with electronic noise and spectrum analyser noise floor*

(i) interferometric signal spectrum
(ii) electronic noise (laser turned off)
(iii) spectrum analyser noise floor

So that it worked in the linear range of the cosine function, the interferometer was locked at half-fringe by controlling the laser drive-current, and hence its λ. This was achieved by low-frequency (100 Hz) dithering of the current, by multiplying the interferometric signal to the dither and lowpass filtering the result. Added to the drive current, this signal locks the interferometer to the half-fringe condition and maximises the output.

From the data in Fig. 3, the noise-equivalent-displacement (*NED*) of the readout system was evaluated as 15 pm/√Hz. As a function of distance, the parabolic dependence was obtained (Fig. 4), in agreement with coherent detection from a rough surface target: the back-injected power varies as z^{-4}, and the signal is proportional to its square root [2].

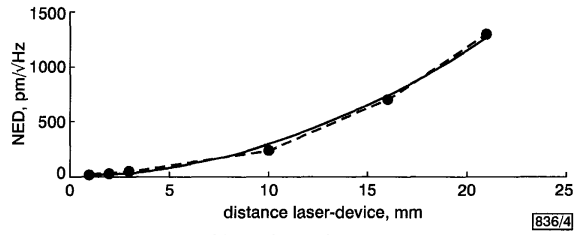

Fig. 4 *NED as function of laser-device distance*

● experimental
——— parabolic fit

System performance: The performance of the hybrid gyroscope can be evaluated from eqn. 1. The parameters of our (non-optimised) device were $\omega_{Rz} = 2\pi \cdot 17$ kHz, Δx up to 6 μm, and Q_z = 2000 at 10^{-1} torr. Therefore, the corresponding noise of the angular velocity $NE\Omega$ is:

$$NE\Omega = \frac{\omega_{Rz}}{Q_z \Delta x} NED \simeq 27\,\mathrm{deg/h}\sqrt{\mathrm{Hz}} \qquad (2)$$

At the noise limit of detection, however, the $NE\Omega$ is much smaller. The two dominant noises are the preamplifier resistance noise (Johnson-noise) and the optical shot-noise. For a 0.3 mW signal, detected by the photodiode, the S/N ratio due to thermal noise is given by $(S/N)\sqrt{B} = (\sigma m P)/\sqrt{(4k_B T/R)}$, where k_B is the Boltzmann constant, T is the absolute temperature and σ is the spectral sensitivity of the photodiode. For R > 100 kΩ, thermal noise becomes negligible compared to quantum-noise, given by $(S/N)\sqrt{B} = mP/(2h\nu P)$ [5]. The attainable *NED* is accordingly evaluated as

$$NED_{shot} = \frac{\lambda}{4\pi} \frac{\sqrt{2h\nu/P}}{m} \simeq 0.3\,\mathrm{pm}/\sqrt{\mathrm{Hz}} \qquad (3)$$

Thus, the hybrid gyro has a potential performance of 0.6 deg/h√Hz for the specimen we have considered, and can be improved further by optimising the mechanical design.

To exploit this performance in a practical system, the zero bias error, which occurs because of the unavoidable coupling of the

mechanical axes and was about 300 deg/h in this case, must also be considered. This zero bias can in principle be cancelled by applying a sine voltage between the substrate and mass (z-axis).

Conclusions: We have proposed and validated a new approach (MOEMS with injection interferometry readout) for gyro sensing of rotation rates down to projected deg/h$\sqrt{}$Hz-accuracy. The approach offers potentially better performance than electrical MEMS gyros, better design flexibility by alleviating the thermal limit [6], and is basically very simple to manufacture.

Acknowledgment: This work was supported by an FAR 60% contract.

4 April 2001
Electronics Letters Online No: 20010520
DOI: 10.1049/el:20010520

M. Norgia and S. Donati (*Dipartimento di Elettronica, Università di Pavia, Via Ferrata 1, I-27100 Pavia, Italy*)

E-mail: norgia@ele.unipv.it

References

1 DONATI, S.: 'Laser interferometry by induced modulation of the cavity field', *J. Appl. Phys.*, 1978, **49**, pp. 495–497
2 DONATI, S., GIULIANI, G., and MERLO, S.: 'Laser diode feedback interferometer for measurement of displacements without ambiguity', *IEEE J. Quantum Electron.*, 1995, **31**, pp. 113–119
3 MERLO, S., and DONATI, S.: 'Reconstruction of displacement waveform with a single-channel laser-diode feedback interferometer', *IEEE J. Quantum Electron.*, 1997, **33**, pp. 527–531
4 ANNOVAZZI-LODI, V., MERLO, S., and NORGIA, M.: 'Measurement on a micromachined silicon gyroscope by feedback interferometry', *IEEE/ASME Trans. Mechatron.*, 2001, **6**, pp. 1–6
5 DONATI S.: 'Photodetectors' (Prentice Hall, Upper Saddle River, NJ, 2000)
6 ANNOVAZZI-LODI, V., and MERLO, S.: 'Mechanical-thermal noise in micromachined gyros', *Microelectron. J.*, 1999, **30**, pp. 1227–1230

Digital integrated circuit using integrated InAlAs/InGaAs/InP HEMTs and InAs/AlSb/GaSb RITDs

P. Fay, J. Lu, Y. Xu, G.H. Bernstein, A. Gonzalez, P. Mazumder, D.H. Chow and J.N. Schulman

The demonstration of the first integrated circuit using monolithically integrated InAs/AlSb/GaSb resonant interband tunnelling diodes (RITDs) and InAlAs/InGaAs/InP high electron mobility transistors (HEMTs) is reported. A D-flip-flop (D-FF) was implemented using the monostable/bistable logic element (MOBILE) circuit architecture, with a measured effective voltage gain in excess of 380. Power dissipation of less than 2.8 mW/gate was measured.

Introduction: For the ultra-fast digital circuits needed for telecommunications, extremely high device speeds and compact circuit topologies are required. The use of resonant tunnelling diodes (RTDs) is promising in this regard, since RTDs exhibit high switching speeds – as low as 1.5 ps [1] – and their unique current-voltage characteristics greatly reduce the circuit complexity needed for logic functions [2 – 5]. Further reduction in power consumption is expected with Sb-based resonant interband tunnelling diode (RITD) circuits due to the low peak voltage that results from the broken-bandgap alignment in InAs/AlSb/GaSb heterostructures [4].

We report the first digital integrated circuit based on monolithic integration of InAlAs/InGaAs/InP HEMTs with InAs/AlSb/GaSb RITDs. A delay flip-flop (D-FF) using the monostable/bistable logic element (MOBILE) circuit architecture [6] has been fabricated and tested. To the authors' knowledge, this is the first report of an integrated circuit fabricated using Sb-based RITDs and InP-based HEMTs.

Heterostructure design and fabrication: The circuits were integrated using a stacked-layer heterostructure in which the HEMT layers were grown first, followed by the RITD layers. The epitaxial layers were grown by molecular beam epitaxy on semi-insulating InP. A δ-doped HEMT heterostructure lattice matched to InP was used. The HEMT heterostructure included a 20 nm InGaAs channel and undoped InAlAs spacer and barrier layers. After the HEMT layers, a 2.5 nm AlAs etch stop layer followed by 50 nm of n^+ InGaAs and an InAs nucleation layer was grown. The RITD heterostructure was grown on this nucleation layer and consisted of a 6 nm undoped GaSb quantum well sandwiched by 1.5 nm thick AlSb barriers and InAs contact layers. The details of the heterostructure growth are described in [7]. Despite the lattice mismatch between the HEMT and RITD layers, good transport properties in the HEMT channel were achieved with a measured sheet carrier concentration of 2.7×10^{12} cm^{-2} and a mobility of 9500 cm^2/Vs at 300 K.

Fig. 1 *Micrograph of core of RITD/HEMT D-FF circuit*

The fabrication process for the RITD/HEMT circuits included wet chemical mesa isolation for both the RITDs and the HEMTs, lifted-off AuGe/Ni/Au and Ti/Au for HEMT ohmic and Schottky contacts, and Cr/Au contacts for the RITDs. Optical lithography was used for all steps except HEMT gate definition; 0.2 μm T-gates were formed by electron-beam lithography in a PMMA/P(MMA-MAA) trilayer resist. Circuit passivation and inter-layer dielectric was realised using benzocyclobutene. Details of the fabrication process have been published previously [7]. A micrograph of the core of the D-FF circuit is shown in Fig. 1.

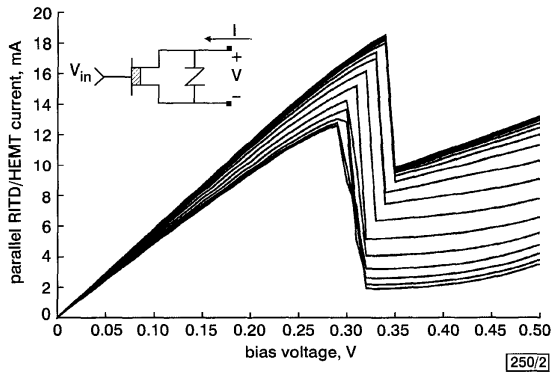

Fig. 2 *Measured current-voltage characteristic of RITD whose effective peak current is modulated by parallel-connected HEMT*

Inset: Schematic diagram of peak-modulated RITD
The HEMT gate-source voltage was stepped from –1.5 to 0 V in 0.1 V steps

Device performance: RITDs fabricated on the integrated RITD/HEMT heterostructure had a peak current density of 17.4 kA/cm^2 and a peak-to-valley ratio of 7.3. The peak voltage was found to be directly related to device area and peak current, indicating that a parasitic access resistance of approximately 9 Ω was present in these devices. This parasitic resistance was due to incomplete removal of the BCB inter-layer dielectric during metallisation via etching.

HEMTs were fabricated on the integrated RITD/HEMT heterostructures and characterised at both DC and microwave frequencies. The threshold voltage was measured to be –0.85 V, with a